

Annual Review of Physical Chemistry
**Ultrafast X-Ray Probes of
 Elementary Molecular Events**

Daniel Keefer,¹ Stefano M. Cavaletto,^{1,2}
 Jérémy R. Rouxel,³ Marco Garavelli,⁴
 Haiwang Yong,¹ and Shaul Mukamel¹

¹Department of Chemistry and Department of Physics and Astronomy, University of California, Irvine, California, USA; email: dkeefe@uci.edu, smukamel@uci.edu

²Current affiliation: Department of Physics and Astronomy, Aarhus University, Aarhus, Denmark

³Université de Lyon, UJM–Saint-Etienne, IOGS, Laboratoire Hubert Curien, UMR CNRS 5516, Saint-Etienne, France

⁴Dipartimento di Chimica Industriale, Università degli Studi di Bologna, Bologna, Italy

Annu. Rev. Phys. Chem. 2023. 74:73–97

The *Annual Review of Physical Chemistry* is online at
physchem.annualreviews.org

<https://doi.org/10.1146/annurev-physchem-062322-051532>

Copyright © 2023 by the author(s). This work is licensed under a Creative Commons Attribution 4.0 International License, which permits unrestricted use, distribution, and reproduction in any medium, provided the original author and source are credited. See credit lines of images or other third-party material in this article for license information.

ANNUAL
REVIEWS **CONNECT**

www.annualreviews.org

- Download figures
- Navigate cited references
- Keyword search
- Explore related articles
- Share via email or social media

Keywords

spectroscopy, conical intersections, X-ray, free-electron laser, photochemistry

Abstract

Elementary events that determine photochemical outcomes and molecular functionalities happen on the femtosecond and subfemtosecond timescales. Among the most ubiquitous events are the nonadiabatic dynamics taking place at conical intersections. These facilitate ultrafast, nonradiative transitions between electronic states in molecules that can outcompete slower relaxation mechanisms such as fluorescence. The rise of ultrafast X-ray sources, which provide intense light pulses with ever-shorter durations and larger observation bandwidths, has fundamentally revolutionized our spectroscopic capabilities to detect conical intersections. Recent theoretical studies have demonstrated an entirely new signature emerging once a molecule traverses a conical intersection, giving detailed insights into the coupled nuclear and electronic motions that underlie, facilitate, and ultimately determine the ultrafast molecular dynamics. Following a summary of current sources and experiments, we survey these techniques and provide a unified overview of their capabilities. We discuss their potential to dramatically increase our understanding of ultrafast photochemistry.

1. INTRODUCTION

1.1. X-Ray and High Harmonic Generation Spectroscopy of Molecules

Elementary chemical events are determined by the coupled motions of molecular nuclei and electrons that happen on the atto- and femtosecond timescales. The monitoring of these ultrafast motions requires spectroscopic tools that use photon and electron beams on a comparable—and preferably shorter—timescale. The advent of novel extreme-ultraviolet (XUV) and X-ray sources has offered new windows into molecular dynamics thanks to their unprecedented brilliance, time resolution, bandwidth, and tunability. X-ray free-electron lasers (XFELs) constitute the fourth generation of X-ray light sources. LCLS (Linac Coherent Light Source) was the first to open to user experiments in 2009 (1), followed by several others around the world, including FERMI (2), SACLA (Spring-8 Angstrom Compact Free Electron Laser) (3), SwissFEL (4), EuXFEL (5), PAL-XFEL (Pohang Accelerator Laboratory XFEL) (6), and DCLS (Dalian Coherent Light Source) (7). Each of these XFELs offers different endstations dedicated to a given type of sample or technique (8). Pulses as short as 280 attoseconds at 905 eV have been reported at the AMO endstation of LCLS (9). Additionally, the bandwidth of XFEL pulses is broad compared with optical ones. The intrinsic self-amplified spontaneous emission (SASE) relative pulse bandwidth $\Delta\omega/\omega_c$ is 10^{-3} – 10^{-4} . The bandwidth depends on the central frequency ω_c (10), which corresponds to a few eV up to tens of eV. It can be further increased using the chirp of the electron beam (11, 12). Broadband XFEL pulses can be used for stimulated X-ray Raman scattering measurements, in which a large manifold of states is probed at once, or for hybrid broadband–narrowband schemes, which combine high temporal and spectral resolutions. On the other hand, techniques that require narrower bandwidths—for example, to achieve element selectivity within a molecular sample—can be achieved by self-seeding of the amplification process (13).

Other types of XUV/soft X-ray sources that show promising capabilities for probing ultrafast molecular dynamics rely on high harmonic generation (HHG). This process exploits the ionization of a (typically noble) gas phase target by an intense IR laser. The ionized electron is accelerated in the strong IR field within a single laser cycle and emits high harmonics upon recollision with the parent ion (14). At present, the resulting harmonics constitute the shortest human-made events and can reach the core K-edge of light elements below 1 keV (15–18). Development efforts to increase the fluence and stability of HHG sources at the carbon and oxygen edges are underway.

Spectroscopic information can be derived either from the HHG process itself or by using the generated pulses for nonlinear measurements. Both HHG and XFELs have enabled novel experimental techniques to study ultrafast molecular dynamics, including advanced XUV and X-ray spectroscopies (19–25), ultrafast X-ray scattering (26–30), Coulomb explosion imaging (31, 32), serial X-ray crystallography (33, 34), and others. These techniques have led to many remarkable experimental breakthroughs on time-resolved imaging of photoinduced dynamics (35), heralding the age of molecular movies (36). In addition, the development of attosecond XFEL and HHG sources has greatly advanced the field of attochemistry, where electronic coherence plays an essential role. Attosecond electron dynamics in molecules has been observed in recent experiments (37–39).

1.2. Monitoring Conical Intersection Dynamics

The passage through a conical intersection (CoIn) is among the most fundamental events across all molecular sciences (40). CoIns show up in any polyatomic system as regions of degeneracy between electronic states. The Born–Oppenheimer approximation, which usually allows for the separate treatment of electronic and nuclear motion, breaks down, and these motions then become strongly coupled since they occur on similar timescales. The molecular system can then

relax nonradiatively between electronic states on very short (femtosecond) timescales, thereby outcompeting other relaxation mechanisms such as fluorescence. The occurrence, topology, and efficiency of CoIn passages therefore determine the outcomes of virtually all photoinduced chemical and biological processes.

The experimental monitoring of CoIns has remained elusive. First, the coupled nuclear and electronic motions in these regions are very fast (femtoseconds) and span a large few-eV energy regime. A broadband pulse that provides excellent temporal resolution may in turn be unable to spectrally resolve the CoIn passage since it covers the entire energy range with its broad spectrum. This is a challenge for spectroscopic techniques that satisfy $\delta\omega\delta t > 1$ because adequate time and frequency resolutions, which are Fourier conjugates, are needed. Second, the direct and unique signatures of CoIns presented here are based on coherences, which are generally much weaker than populations. To date, the presence of CoIns in optical pump-probe spectra is inferred from ultrafast decay rates (41) or rapid changes in characteristic absorption lines (42), or from the analysis of photofragments (43). With subfemtosecond XFEL pulses (44, 45), and with ever-shorter and more coherent HHG pulses, the temporal resolution of this probing scheme has reached the few-femtosecond regime (46, 47).

Accompanying and inspiring this experimental progress are theoretical proposals that design the next generation of measurements and demonstrate novel ways to exploit the increasing capabilities of light sources. In the past few years, researchers have proposed an arsenal of new techniques that tackle the fundamental challenge of detecting CoIns from different angles. The targeted signatures directly rely on coherences that form during the CoIn passage. These techniques include X-ray stimulated Raman spectroscopy (48–51), time-resolved X-ray diffraction (TXRD) (52–55), ultrafast electron diffraction (UED) (56, 57), and time-resolved photoelectron spectroscopy (tr-PES) (58, 59). A wealth of information about the CoIn itself is accessible from the recorded spectra, such as energy splittings of adiabatic states (49) and spatial distributions of electron transition densities (55). Once experimentally realized, these techniques should enhance our understanding of CoIns in general and of specific functional molecules. For example, they already act as the operational principle in photoswitchable pharmacology (60) and materials (61), where a parametric understanding of on and off states dominates. Modern spectroscopies based on the principles outlined here may reveal that it is rather a coherent superposition of states—analogue to Schrödinger’s cat—with CoIns mediating the dynamical evolution. This review offers a summary of recently developed ultrafast spectroscopic techniques that specifically target CoIns via a new family of signatures based on vibronic coherences created during the CoIn passage (**Figure 1**).

1.3. Simulation Protocols for Molecular Dynamics and Their Signals

A wide variety of theoretical approaches have been used to simulate the dynamics of molecular systems, depending on the process and quantities of interest. These range from classical parameterized force fields that propagate nuclear point charges according to Newton’s equations of motion to exact nuclear quantum dynamics by the time-dependent Schrödinger equation (TDSE) (62). Different flavors of semiclassical approaches combine both worlds or find more approximate treatments of quantum mechanical motions; among the most prominent examples are Tully’s fewest-switches surface hopping (63, 64), ab initio multiple spawning (65) and cloning (66), and the multiconfigurational time-dependent Hartree (67).

All signals presented in this review are based on the total molecular wave function $\Psi(q, r, t)$, which depends on a set of $q \equiv (q_1, \dots, q_N)$ nuclear degrees of freedom, electronic degrees of freedom r , and time t . Expanded in adiabatic electronic states labeled k , it reads

$$\Psi(q, r, t) = \sum_k \psi_k(q, t) \phi_k(r; q), \quad 1.$$

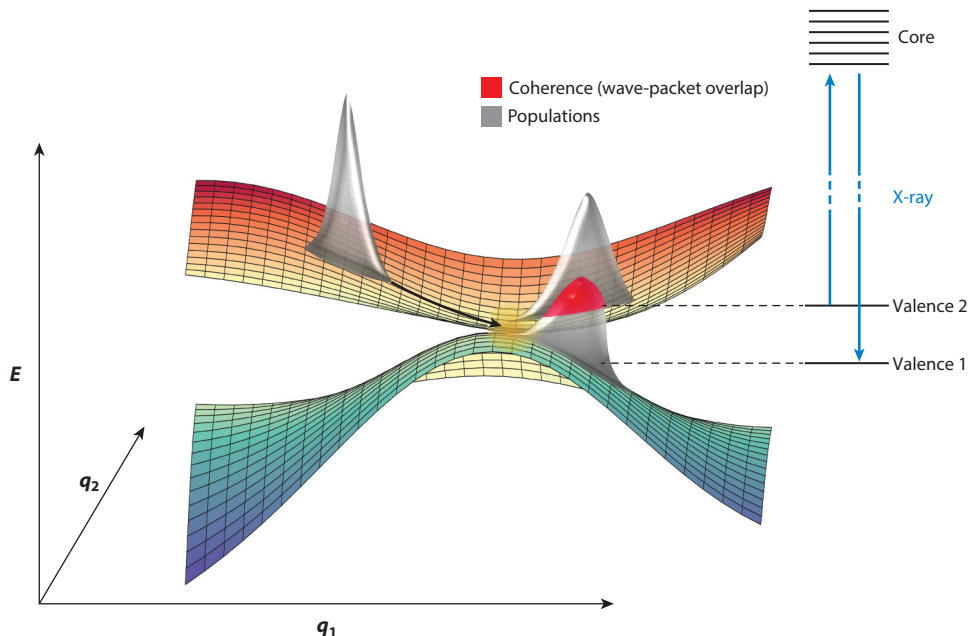


Figure 1

Sketch of a nuclear wave packet passing through a conical intersection (CoIn). The conformational subspace consists of two nuclear degrees of freedom, q_1 and q_2 , that lift the electronic degeneracy. Before the CoIn, the wave packet is only in one electronic state. After bifurcation, there is wave-packet overlap (*red*) between two electronic states, that is, a vibronic coherence. These cause unique signatures in time-resolved X-ray signals that are different from the populations (*gray*). An exemplary X-ray probe process is sketched as an off-resonant stimulated Raman transition between the electronic states forming the CoIn.

where $\psi_k(q, t)$ is the nuclear wave function and $\phi_k(r; q)$ is the electronic wave function. The molecular dynamics is obtained by propagating $\psi_k(q, t)$ in time according to the TDSE (62), providing a robust framework for the calculation of spectroscopic signals that depend on molecular quantities like dipoles and charge densities (recently reviewed extensively in Reference 68). A quantum mechanical treatment of nuclear dynamics is essential to properly account for CoIn passages and, thus, to capture the signatures that are based on them. An approaching nuclear wave packet, initially located in electronic state 1, partly relaxes into state 2, causing a nonvanishing overlap of both nuclear wave packets $\langle \psi_1 | \psi_2 \rangle$, that is, a coherence. When simulating spectroscopic signals of ultrafast molecular dynamics in excited states, and especially when targeting signatures that stem from the CoIn passage itself, it is essential to properly account for these coherences. This is naturally given by traditional nuclear quantum dynamics and is partly accessible in other frameworks like *ab initio* multiple spawning and cloning, but is missing in, for instance, fewest-switches surface hopping.

2. PROBING COHERENCE DISTRIBUTIONS AT CONICAL INTERSECTIONS

2.1. TRUECARS and Vibronic Coherence Spectrograms

Transient redistribution of ultrafast electronic coherences in attosecond Raman signals (TRUECARS) (48–50) is a particularly promising signal for the observation of CoIns that

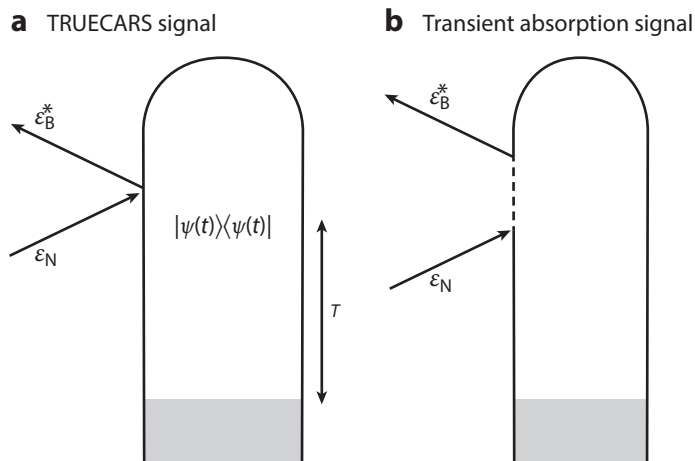


Figure 2

Loop diagrams for (a) TRUECARS and (b) transient absorption signals. Abbreviation: TRUECARS, transient redistribution of ultrafast electronic coherences in attosecond Raman signals.

exploits the unique capabilities of novel X-ray sources. The technique uses a hybrid broadband–narrowband X-ray probe field at variable time delay after optical excitation of the molecular sample (**Figure 2**). The X-ray probe pulses induce a stimulated Raman process between valence electronic states (compare with **Figure 1**). The signal appears only once there is a nonvanishing overlap between nuclear wave packets in two electronic states—that is, a vibronic coherence—as is generated at, for example, a CoIn due to wave-packet bifurcation (**Figure 1**). The total rate of change of the photon number in the broadband field, which is the detection mode in the TRUECARS signal, is zero since the probe field is off-resonant to any material transitions and thus may not be absorbed. Only the frequency dispersion of the broadband field after interaction shows up, exhibiting gains and losses at positive and negative Raman shifts ω , corresponding to a redistribution of photon energy (**Figure 3**). A gain at $\omega < 0$ and a loss at $\omega > 0$ mean that the field is depositing energy into the system, corresponding to a Stokes-type process. A loss at $\omega < 0$ and a gain at $\omega > 0$ imply that the field is receiving energy from the system, corresponding to an anti-Stokes process. The signal oscillates between these two scenarios with the phase of the vibronic coherences. The high temporal resolution and a broad frequency bandwidth make TRUECARS a unique probe of nonadiabatic dynamics that has no optical equivalence.

TRUECARS can be carried out in a variety of detection modes depending on the probe used. First, the probe can be hybrid—that is, composed of two phase-locked pulses with different temporal and spectral characteristics—or not. Second, the probe pulses must be phase-locked to prevent signal cancellation upon averaging. Third, TRUECARS can be detected with attosecond pulse trains, as demonstrated recently (69). Finally, the stimulated Raman process should be off-resonant. When the X-ray pulse is resonant to the core states in the molecule, as in attosecond transient absorption spectroscopy, contributions from state populations emerge and TRUECARS loses its selectivity to coherences.

In its original proposition, an off-resonant hybrid broadband–narrowband probe was employed in a heterodyne detection scheme. The nuclear wave packet is excited by an optical pulse and undergoes nonadiabatic dynamics. To keep the discussion general, this wave packet $|\psi(t)\rangle$ is kept as is, but it could also be expanded into, for instance, a diabatic basis. After a delay T , a hybrid probe induces an off-resonant stimulated Raman transition between the two potential energy surfaces

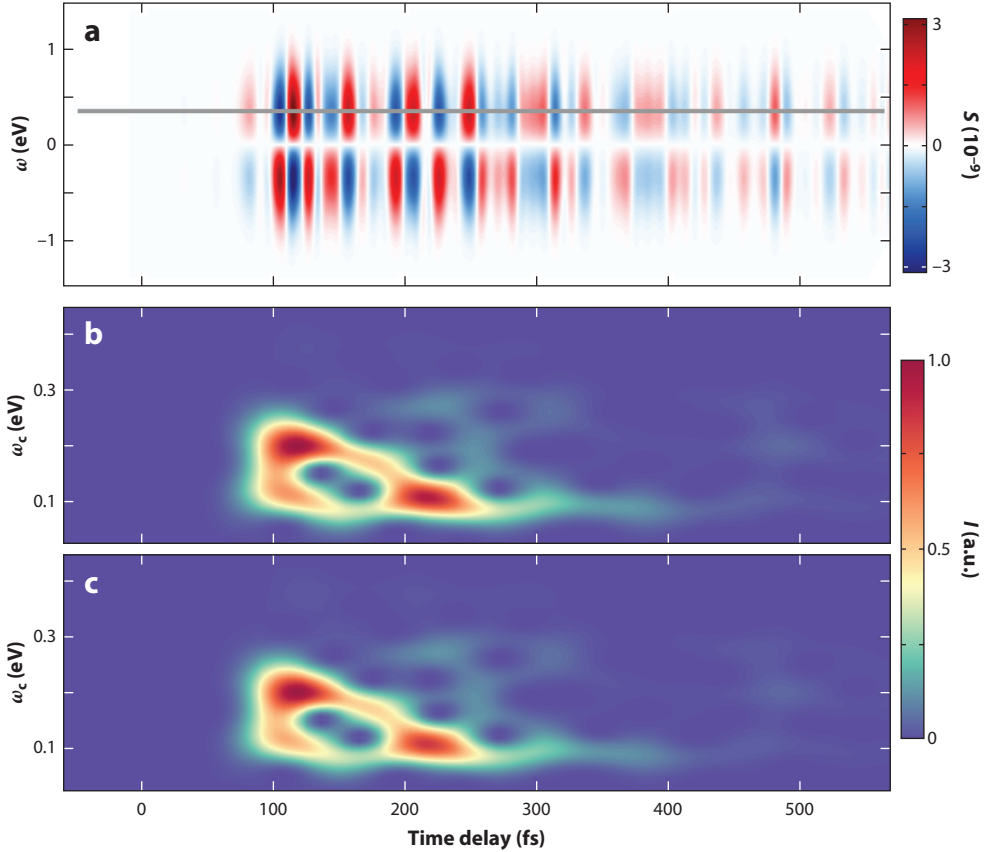


Figure 3

(a) TRUECARs signal (Equation 2) of uracil photorelaxation (49) initiated by a 20 fs Gaussian pump centered around $t = 0$ and probed by a hybrid broadband–narrowband X-ray probe field. The signal emerges only around 80 fs, when the molecule starts to undergo CoIn passage. (b) Spectrogram of the TRUECARs signal according to Equation 4. $S(t)$ is a temporal trace of the signal in panel a (gray line). (c) Same spectrogram, but with $S(t)$ taken as the integral of positive Raman shifts. It has a shape almost identical to that in panel b, indicating that precise spectral resolution is not needed, provided that one can separate between positive and negative Raman shifts. The frequency information can be recovered at the postprocessing stage. Abbreviations: CoIn, conical intersection; TRUECARs, transient redistribution of ultrafast electronic coherences in attosecond Raman signals.

(PESs). This hybrid probe is made of broadband \mathcal{E}_B and narrowband \mathcal{E}_N pulses. The former ensures an attosecond temporal resolution of the recorded event and a broad spectral window for the observation of the signal, whereas the latter provides the required frequency resolution to detect the evolution of the coherence generated at the CoIn as the molecular wave packet spans different regions on the PESs. The signal can be read from the loop diagram in **Figure 2a** and is given by the heterodyne detection of the dispersed broadband pulse:

$$S(\omega, T) = 2\text{Im} \int dt e^{i\omega(t-T)} \tilde{\mathcal{E}}_B^*(\omega) \mathcal{E}_N(t-T) \langle \psi(t) | \hat{\alpha} | \psi(t) \rangle. \quad 2.$$

In contrast, the transient absorption signal (70) can be read from the diagram in **Figure 2b** and is given by

$$S(\omega, T) = 2\text{Re} \int dt \int_0^{+\infty} ds_1 e^{i\omega(t-T)} \tilde{\mathcal{E}}_B^*(\omega) \mathcal{E}_N(t-s_1-T) \langle \psi(t) | \hat{V} \hat{G}(s_1) \hat{V}^\dagger | \psi(t-s_1) \rangle, \quad 3.$$

where s_1 is the propagation time in the core excited state and V is the electronic transition dipole operator. The resonant interaction adds an extra molecular propagator $G(s_1)$ into the correlation function. Transient absorption is well established in the optical regime and straightforwardly transferable to X-rays, which is why it is commonly used here as well. In contrast to TRUECARS, usually both interactions (**Figure 2b**) occur with the same single probe pulse. CoIn passages show up in X-ray transient absorption spectra as rapid changes in absorption lines stemming from specific valence-to-core transitions (71, 72). The added element selectivity obtained from the resonant core excitation can be used to disentangle complex electronic dynamics that includes multiple CoIns. However, transient absorption is not an exclusive probe of molecular coherences.

There is unique information in the TRUECARS signal that can be extracted directly from the recorded spectrum. The Raman shift ω observed by frequency-dispersing the broadband $\tilde{\mathcal{E}}_{\text{B}}^*(\omega)$ field directly corresponds to the energy shift between the adiabatic states forming the vibronic coherence (compare with **Figure 1**). In Reference 48, where a localized nuclear wave packet traverses a model CoIn, the main feature of the TRUECARS signal was observed closer to zero Raman shift, at $\omega = 0$ when the wave packet was in the vicinity of the CoIn, and at increasing ω when the wave packet evolved away from the CoIn. Any vibronic coherence will in principle show up in the TRUECARS signal, provided that $\tilde{\mathcal{E}}_{\text{B}}^*(\omega)$ has a broad enough bandwidth, but only those stemming from a CoIn will be centered around $\omega = 0$. In a real molecular system (49), nuclear wave packets may be much less localized. A delocalized coherence that travels around the CoIn may exhibit constant Raman shifts close to $\omega = 0$, in which case less dynamical information can be extracted simply by inspecting ω .

Additional information can be derived by analyzing the temporal oscillations in the TRUECARS signal. The coherence between the adiabatic states propagates with a time-dependent dynamical phase that corresponds to their energy difference (48, 49). Thus, the instantaneous frequency—and the energy splitting between the adiabatic states—can be accessed with a Wigner transformation or a temporal gating operation at the postprocessing stage (49). The equation for the latter corresponds to a (cross-correlation) frequency-resolved optical gating (FROG)/XFROG measurement (73, 74) and reads

$$I(\omega, T) = \left| \int_{-\infty}^{\infty} dt S(t) E_{\text{gate}}(t - T) e^{-i\omega t} \right|^2, \quad 4.$$

where E_{gate} is an arbitrarily chosen gating function and $S(t)$ is a temporal signal trace taken at constant ω . In order to calculate this spectrogram of the TRUECARS signal, excellent temporal resolution is desirable, but the frequency resolution does not need to be high. As demonstrated in **Figure 3**, it is sufficient to separate positive and negative Raman shifts, as integration over the complete ω range will reduce the signal to zero.

Following the initial demonstration on a vibronic coupling model Hamiltonian (48), we simulated the TRUECARS signal for different molecular processes. In addition to uracil (49) and 4-thiouracil (75), the TRUECARS spectrogram has proven valuable in revealing the effects of initiating photochemistry through CoIns by two entangled photons on azobenzene isomerization (76). TRUECARS can also be instrumental in probing coherences in fused aromatic units (50) or dendritic molecules (77), which are promising candidates as building blocks for optoelectronic materials. Designing molecules with long-lasting coherences that can compete with decoherence mechanisms and incoherent scrambling pathways and survive multiple CoIn passages is an important step toward increasing the energy transport properties of the macroscopic devices they will be used in. As was recently demonstrated, TRUECARS can reliably give insight into whether coherences are persistent (50) and the molecule is a suitable candidate for further testing, or whether modifications need to be made because of dominant incoherent scrambling pathways (77) that manifest as a rapid decay of the signal.

The major experimental challenge of TRUECARS is generating stable X-ray pulse pairs with a controllable relative phase, which is still very difficult and is the subject of extensive research efforts (78). Alternatively, the stochastic nature of XFELs can be used in a covariance-based measurement to recover coherent information, as discussed below in Section 4. TRUECARS can also be detected with attosecond pulse trains originating from an HHG process (69). This study also included the contribution of vibrational coherences to the TRUECARS signal, which can be more or less pronounced than the electronic coherences depending on the symmetry of the model used. Because the vibrational coherences oscillate much more slowly than the electronic ones, a Wigner or XFROG spectrogram could be used to disentangle them (69).

TRUECARS can be regarded as the high-energy counterpart to coherent anti-Stokes Raman scattering (CARS). Both techniques use a high-frequency pulse to probe a manifold of states lying at a lower energy. Time-resolved CARS uses optical pulses to probe vibrational wave packets, while TRUECARS uses XUV or X-rays to probe valence electronic dynamics. Additionally, CARS usually generates vibrational coherences during the pump process, while for TRUECARS, additional electronic coherences naturally appear during the CoIn passage. These are energetically separated from the electronic coherences during the pump, since they are centered around a 0 eV Raman shift (corresponding to the vanishing energy gap at the CoIn) in the frequency-resolved spectrum, as opposed to a few eV during the excitation.

2.2. Time-Resolved X-Ray and Electron Diffraction

Ultrafast X-ray and electron diffraction are complementary techniques for monitoring transient molecular structures. **Figure 4** illustrates the general principle of diffraction experiments, and **Figure 5** shows the loop diagrams. An optical pump pulse excites the molecular sample and prepares a superposition of nonstationary states. At variable time delay after the pump, a femtosecond X-ray or electron pulse arrives at the sample and is scattered off the current geometry. A diffraction pattern is recorded at the detector as a function of the vector $\mathbf{q} = \mathbf{k}_s - \mathbf{k}_p$, which is the scattering momentum transfer between the incident and scattered photons or electrons with wave vectors

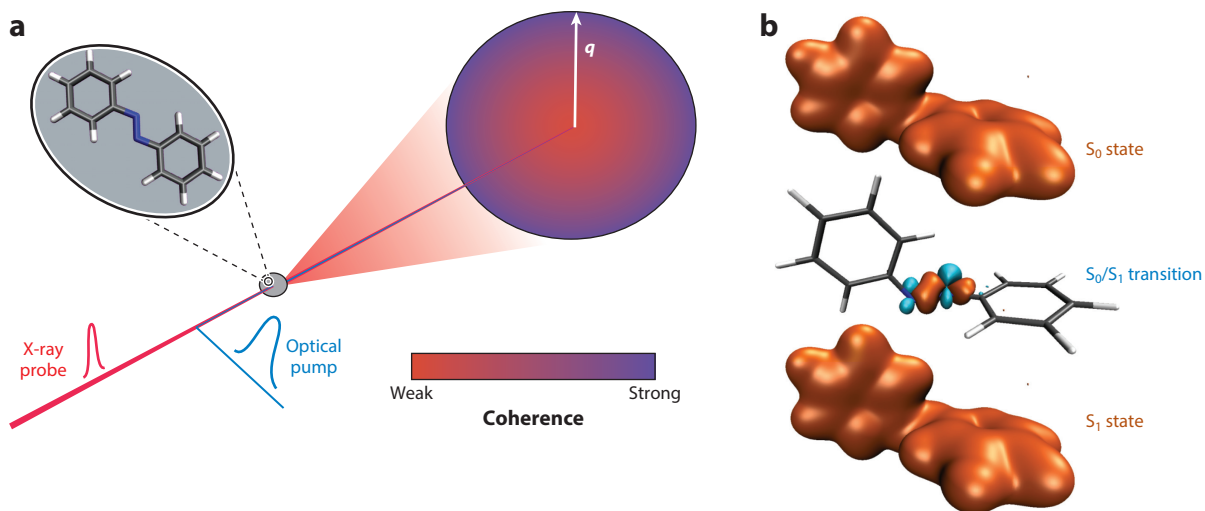


Figure 4

(a) Diffraction experiment schematic. The color gradient on the pattern indicates where the conical intersection is strong. (b) Orbital pictures with total versus transition densities to get across the point of spatial extent and q range.

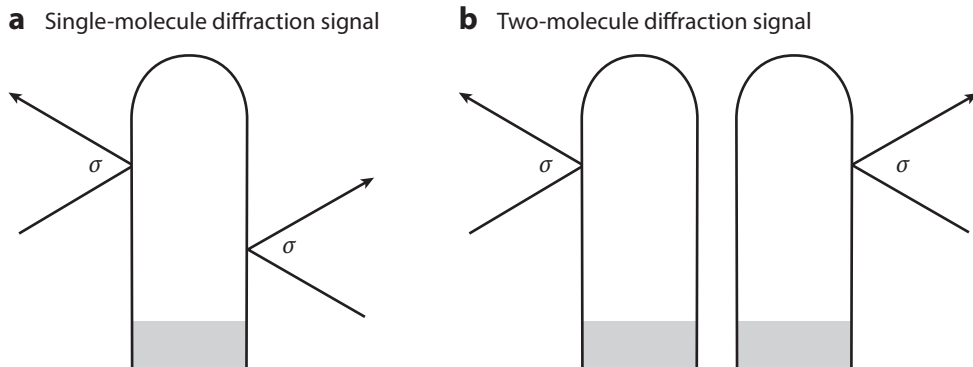


Figure 5

Loop diagrams for (a) the single-molecule and (b) the two-molecule diffraction signal. σ is the electronic charge density for time-resolved X-ray diffraction and the total charge density for ultrafast electron diffraction.

\mathbf{k}_p and \mathbf{k}_s . A temporal series of such diffraction patterns then reveals structural changes during the molecular dynamics, with many different signatures that are explained below.

Comparisons of UED and TXRD have been discussed extensively (56, 79–81). There are several important differences between X-ray diffraction and electron diffraction. First, TXRD probes the electronic charge density, whereas UED measures the total (electronic + nuclear) charge density (82). Second, typical X-ray wavelengths are much longer than the de Broglie wavelength of electrons, so that X-ray scattering patterns can reveal more detailed information at small scattering angles, while electron diffraction can measure signals at very large scattering angles. Third, while X-ray diffraction uses Thomson scattering of X-rays (83), electron diffraction is based on Rutherford scattering of electrons (84). Both Thomson and Rutherford scattering are elastic scattering. The key difference is that the former refers to scattering of electromagnetic radiation (i.e., photons) by a free charged particle through the electromagnetic dipole radiation, while the latter refers to scattering of charged particles (electrons) by a free charged particle through the Coulomb interaction. These are two distinct physical processes that have very different cross sections. Although the Rutherford scattering cross section is much larger than the Thomson one, space-charge effects make it difficult to maintain short pulse durations of electrons.

TXRD has recently achieved femtosecond resolution thanks to ultrashort XFEL pulses (1, 85, 86). Similarly, relativistic MeV electron pulses (87, 88) have pushed UED into the femtosecond regime. Both TXRD and UED are able to follow structural changes, as demonstrated for the ring opening of cyclohexadiene (26, 89, 90) and the photodissociation of trifluoroiodomethane (91) and trimethylamine (92). In these measurements, signatures of CoIns are inferred by combining the data analysis with *ab initio* simulations. Advanced data processing of TXRD signals on the *p*-coumaric acid chromophore in photoactive yellow protein (93) has made it possible to determine the topography of the CoIn crossed upon photoexcitation.

A typical TXRD measurement records the amplitude squared of the Fourier transform of the electronic charge density, $|\sigma^{\text{el}}(\mathbf{q})|^2$, where \mathbf{q} is the scattering momentum transfer. UED similarly measures the total (electronic + nuclear) charge density, $|\sigma^{\text{tot}}(\mathbf{q})|^2 = |\sigma^{\text{el}}(\mathbf{q}) + \sigma^{\text{nuc}}(\mathbf{q})|^2$. As a consequence, all electrons contribute to the signal. In ultrafast molecular dynamics, only a few electrons contribute to the nonadiabatic passage, while the others serve as spectators or follow adiabatically the nuclear dynamics. In fact, the signal is generated mostly by the numerous core electrons, while the few valence electrons have a smaller contribution. However, TXRD and

UED also offer various parameters, such as the detected momentum transfer and the pulse bandwidths and durations that can be used to extract the desired information.

TXRD and UED signals are composed of multiple interaction pathways (52, 56, 94–97), some of which are specific to electronic coherences. These contributions possess mixed elastic + inelastic scattering contributions. While the total ultrafast diffraction signals scale with the number of electrons in the molecule, the mixed terms do not scale with it and usually get buried under the other, stronger contributions.

The impulsive single-molecule TXRD signal (or, equivalently, an ensemble of randomly noninteracting molecules) is given by

$$S_{\text{TXRD}}(\mathbf{q}, T) \propto \text{Re}\langle\psi(T)|\hat{\sigma}^{\text{el}}(-\mathbf{q})\hat{\sigma}^{\text{el}}(\mathbf{q})|\psi(T)\rangle. \quad 5.$$

Similarly, the impulsive UED signal on a single molecule is given by

$$S_{\text{UED}}(\mathbf{q}, T) \propto \frac{1}{q^4} \text{Re}\langle\psi(T)|\hat{\sigma}^{\text{tot}}(-\mathbf{q})\hat{\sigma}^{\text{tot}}(\mathbf{q})|\psi(T)\rangle. \quad 6.$$

Detailed expressions for the various contributions are given in Reference 56, and the general loop diagram for the single-molecule diffraction signal is shown in **Figure 5a**. By expanding the wave function in electronic eigenstates, each of the two signals can be broken down into multiple contributions. Among them, terms of the form $\text{Re}\langle\chi_g(T)|\sigma_{eg}(-\mathbf{q})\sigma_{ee}(\mathbf{q})|\chi_e(T)\rangle$ carry direct signatures of CoIns. The inverse Fourier transform of these contributions provides a spatial image of the CoIn.

Both TXRD and UED have been simulated for azobenzene photoisomerization (53, 98), a textbook photochemical reaction that connects stable *cis* and *trans* isomers (compare with **Figure 4**, which shows a transition structure between both isomers with a 90° angle between the carbon rings). Optical switching between these two can be achieved by using visible light with different wavelengths. In addition to being a prototype model photoswitch, azobenzene-based molecules are used in numerous applications ranging from photopharmacology and optogenetics (60) to materials with different properties and purposes (61). Temporally and spatially resolving the CoIn dynamics in such molecules are thus crucial to gain fundamental insight and for molecular design applications.

TXRD patterns contain coherence signatures that are directly related to the transition densities associated with the CoIn passage (53). This spatial information is exclusive to scattering measurements and is not accessible with the other signals discussed here, such as TRUECARs and tr-PES. The coherence contribution is much weaker than the ones from populations and is therefore buried in the total diffraction signal. With increasing momentum transfer, however, the relative strength of this signature in the total signal is increased. The reason is shown in **Figure 4**. All 96 electrons of azobenzene contribute to the electronic-state densities, which are responsible for elastic scattering. This is what is conventionally recorded in diffraction patterns. The coherence signature is based on the transition densities between the electronic states, where only one electron—the one associated with the electronic transition, in this case originating from a nitrogen lone pair—contributes. Since this transition density is more confined in real space than the state densities, its relative strength increases at large q values in momentum space. This general feature applies to the valence-state photochemistry of most molecules. A frequency-resolved TXRD measurement could similarly highlight the contribution from transition densities (55). This measurement relies on the fact that the fast oscillating coherence dynamics leads mostly to inelastic scattering, whereas the slower population dynamics is associated with elastic scattering. These two terms could be separated by frequency-dispersing the signal at each pixel point in the detector, or by a time–frequency analysis based on, for instance, FROG-like spectrograms. This topic is discussed further in Section 4. Next-generation X-ray sources provide higher pulse energies

that can record increasing momentum transfer amplitudes, which will lead to new possibilities for diffractive imaging of CoIns. Section 4 also discusses how stochastic sources, as they exist today, can already help retrieve this information.

The TXRD signal has been simulated for the photorelaxation of 4-thiouracil (75). Unlike azobenzene, this molecule does not undergo significant structural changes such as isomerization but rather relaxes back to the original ground-state minimum. Accordingly, the TXRD patterns vary less with time. An exception is the coherence contribution stemming from the CoIn, which again exhibits dynamical features due to the oscillations in the electron transition densities in real space.

As discussed in more detail in References 56 and 98, the UED signal contains additional contributions to TXRD due to scattering from the total (nuclear + electronic) charge density rather than from the electronic one alone. Because the nuclear charge densities and atomic core electrons are typically more confined in space compared with more-diffuse valence electrons that are responsible for chemical bonding, they can be separated in UED experiments that record them simultaneously (99). In addition to these contributions and the coherence signatures from CoIns, as discussed in the case of TXRD, there are mixed nuclear + electronic signatures that are unique to UED (56, 98). In terms of the loop diagram in **Figure 5**, this means that the interaction on one branch occurs with the nuclear charge density and that the one on the other branch occurs with the electronic one. This unique signature provides a new level of sensitivity with respect to CoIns, since their unique feature is a strong coupling of nuclear and electronic degrees of freedom.

We recently demonstrated that by combining TXRD and UED (100), one can isolate the purely nuclear contributions to the diffraction patterns. This finding is especially intriguing because it provides direct information about nuclear wave packets—that is, the motions of atoms and molecules—compared with the more indirect spectroscopic probes that detect electronic properties such as dipoles or polarizabilities. To isolate the contributions, both TXRD and UED signals must be heterodyned and carefully normalized (100), a highly challenging experimental proposition. The combined technique can provide unique direct insight into molecular wave-packet dynamics that is not accessible by any other means.

2.3. Time-Resolved Photoelectron Spectroscopy

Photoelectron spectroscopy relies on ionization as the main process responsible for the signal (101). In tr-PES, time-resolved information is obtained by varying the arrival time of an ionizing probe pulse and by measuring the kinetic energy distribution of the emitted photoelectrons (102–104); recent advances have employed XUV (105, 106) and X-ray pulses (25, 107). In contrast, for the stimulated X-ray Raman and diffraction techniques discussed above, photoionization due to the X-ray probe acts as a competing process that should be minimized. tr-PES signals contain strong contributions from the populations of the molecular states, and most theoretical methods interpret photoelectron spectra in terms of a semiclassical Fermi's golden rule, where the role of molecular coherences is entirely neglected (108–110).

Reference 58 proposed the idea of accessing electronic coherences at CoIns via tr-PES. The tr-PES signal is represented by the diagram in **Figure 6a**. It depends on the emitted photoelectron energy ϵ and the arrival time T of the ionizing X-ray pulse, and is expressed as

$$S(\epsilon, T) = 2\text{Re} \int dt \int_0^\infty dt_1 \mathcal{E}^*(t - T) \mathcal{E}(t - t_1 - T) e^{-i\epsilon t_1} \sqrt{2\epsilon} \int d\Omega_{\mathbf{k}_e} \langle \psi(t) | \hat{V} \hat{G}(t, t - t_1) \hat{V}^\dagger | \psi(t - t_1) \rangle, \quad 7.$$

where the pulse $\mathcal{E}(t)$ and the wave function $|\psi(t)\rangle$ of the neutral molecule precede the X-ray ionization. \hat{V}^\dagger is the dipole operator leading from the neutral molecule in state $|I\rangle$ to the cation in

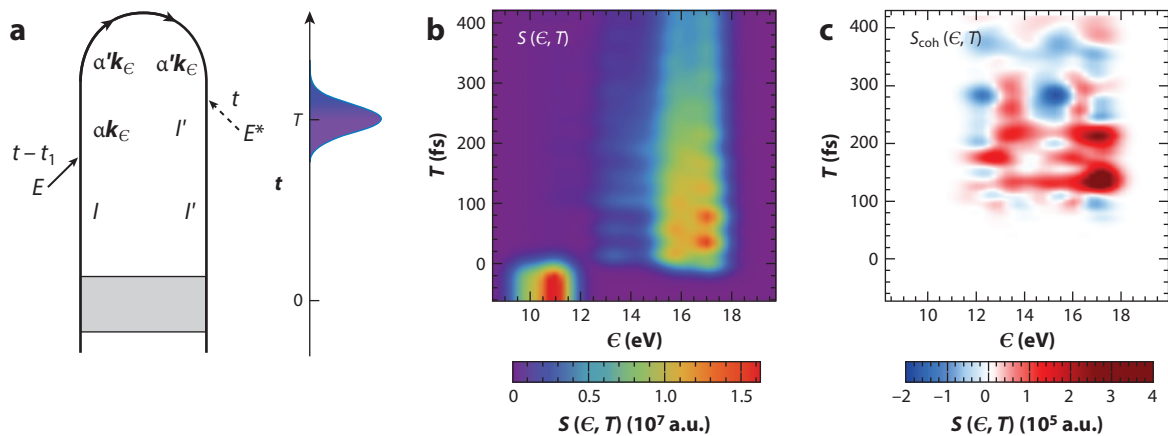


Figure 6

(a) Loop diagram of the tr-PES signal. (b) Total tr-PES signal according to Equation 7 during uracil photorelaxation. (c) Signal stemming purely from the coherence emerging at the initial conical intersection around 80 fs. Abbreviation: tr-PES, time-resolved photoelectron spectroscopy. Figure adapted from Reference 59.

state $|\alpha\rangle$ and the free electron in state k_ϵ (**Figure 6a**). $\hat{G}(t, t - t_1)$ describes the free evolution of the cation between the left and right interactions in **Figure 6a**, while the corresponding evolution of the emitted photoelectron is given by $e^{-ie t_1}$. Here, we focus on the energy-resolved signal in Equation 7, which is obtained by integrating over the solid angle $d\Omega_{k_\epsilon}$ at energy ϵ . We note that angular-resolved tr-PES, based on a moment analysis of the photoelectron angular distribution, was recently implemented to separate electronic coherences from population dynamics (111).

When the neutral molecule is in a coherent superposition state $|I\rangle\langle I'|$, the same broadband pulse can induce ionization, on both the left and right branches, to the final state $|\alpha\rangle\langle\alpha|$. The amplitude of this contribution is directly related to the magnitude of the molecular coherence. Like TRUECARs, the X-ray probe bandwidth will determine the temporal and spectral resolutions of the tr-PES signal. Proposals to improve the temporal and spectral resolutions by using trains of attosecond pulses have recently been made (112).

The tr-PES signal was recently computed for the nonadiabatic dynamics of photoexcited uracil undergoing passage through a CoIn (59). The predicted contributions stem from the molecular coherences emerging at the CoIn between the excited S_2 state and the optically dark S_1 state in neutral uracil. **Figure 6b** shows the total tr-PES signal, and **Figure 6c** shows the purely coherent contribution. For ultrashort attosecond pulses, strong tr-PES features can be distinguished because of the coherence between the ground S_0 and the bright S_2 excited state. Although the frequency resolution of the photoelectron signal was eroded for short broadband pulses, good time–frequency resolution was recovered at the data processing stage via Wigner or FROG-like spectrograms (Equation 4). These are analogous to the TRUECARs spectrogram discussed in Section 2.1. Specifically, by scanning the spectrogram at sufficiently high frequencies, one can highlight the role of the coherence emerging at the CoIn and separate it from the population background. This is crucial because the coherence signature is two orders of magnitude smaller than the population and is thus hidden in the total signal (**Figure 6**).

3. TIME-DEPENDENT MOLECULAR CHIRALITY

Circularly polarized light has long been highly valuable for probing molecular chirality. Ultrashort XUV and X-ray sources also provide accurately controllable circular polarization of the pulses

(113, 114). Chiral molecules are objects that are not superimposable with their mirror images. The two are referred to as enantiomers. Such molecules are highly important for biochemistry, drug synthesis, and consumer chemistry. However, standard spectroscopic techniques cannot distinguish between two enantiomers, and chiral discrimination usually shows up as a small correction on top of an achiral background. The chiral contribution can then be extracted by taking the difference of observables acquired with left and right circular polarization. These could be, for instance, absorption [circular dichroism (CD)] or Raman scattering [Raman optical activity (ROA)]. Developing more sensitive and informative chiral signals is essential for better understanding this phenomenon on the fundamental level and for formulating design principles for synthesis and application. Because the excited-state dynamics of chiral molecules can exhibit interesting features that determine, for instance, the photochemical enantiomeric yield, this issue is inherently linked to CoIns. Below, we survey novel ways of probing chiral molecular properties and dynamics with XUV and X-ray pulses.

One way to exploit X-ray sources is through their element specificity. Increasing the distance between an X-ray chromophore and the chiral molecular center (more correctly named the stereogenic center) decreases the strength of the X-ray CD signals resonant with the chromophore (115). This picture is complicated by the fact that some molecules have multiple stereogenic centers (e.g., menthol) or have a globally chiral geometry without a stereogenic center (e.g., helicenes or 1,1'-bi-2-naphthol). The use of resonant X-rays as a probe in CD and ROA signals provides additional structural information linking the stereogenic center and the probed atom.

Ultrashort pulses enable the design of time-resolved experiments that monitor chiral dynamics. We consider multiple prototypical situations. First, a stable chiral molecule in its ground state is excited and its subsequent dynamics is followed using a chiral-sensitive signal. Repeating the experiment at different core edges allows one to reconstruct how each atom (or group of degenerate atoms) is influenced by normal coordinates involving chiral nuclear motions. tr-XCD experiments have been conducted at the carbon K-edge of ibuprofen and chloroquine (116). Second, some molecules are achiral in their ground state and become chiral in their excited state. A prototypical example is formamide, which is planar and achiral in its ground state and can become chiral in its first excited state due to its pyramidalization. Simulations have shown that tr-XCD can accurately follow the molecular dynamics (117) and is sensitive to the mean position of the nuclear wave packet on the molecular PES. Finally, the potential barrier between the two enantiomers can be low, leading to racemization dynamics. When this happens in the excited state, and particularly when nontrivial pathways involving CoIns can reach a given final product, the selectivity of X-rays could prove invaluable. For example, *cis*-azobenzene has two enantiomers, *cis*-(*P*)-azobenzene and *cis*-(*M*)-azobenzene, and its relaxation between the two upon photoexcitation of *trans*-azobenzene into the S_1 state involves a CoIn (118).

The techniques described above rely on dichroic measurements, which probe higher multipoles in the radiation–molecule coupling. Recently, two other approaches have been demonstrated. The first relies on signals existing in the electric dipole coupling. To obtain chiral discrimination, the interaction must be even-order nonlinear in the perturbative field (119). The source of the chiral discrimination arises from the fact that even-order susceptibilities vanish in centrosymmetric media, a randomly oriented ensemble of molecules in this case. Chirality breaks the centrosymmetry and allows for chirality-sensitive signals. Other electric dipole coupling alternatives include photoelectron circular dichroism (PECD) (120) and chiral HHG (121), in which the chiral interaction exists in the electric dipole coupling because transition dipoles are complex for transitions into a continuum. Large asymmetry factors have been reported, and this detection mode has been used in multiple time-resolved experiments.

Table 1 Chiral-sensitive signals sorted by their coupling with matter

Chiral signals			
	Multipolar	Electric dipole	Minimal coupling
Static	XCD XROA	SFG/DFG cHHG PECD	HD HROA
Time-resolved (tr)	tr-XCD tr-ROA	tr-PECD tr-cHHG	tr-HD tr-HROA

Abbreviations: cHHG, chiral high harmonic generation; DFG, difference-frequency generation; HD, helical dichroism; HROA, helical Raman optical activity; PECD, photoelectron circular dichroism; SFG, sum-frequency generation; XCD, X-ray circular dichroism; XROA, X-ray Raman optical activity.

The second approach employs the orbital angular momentum (OAM) of light, which has also been proven to be chiral sensitive (122, 123). A light beam with OAM, also called a vortex beam, possesses a wave front that twists along the beam propagation, independently of the beam polarization state. Such beams contain a phase twist that engages spatially with the molecular chirality; in contrast, circular polarization relies on the spin angular momentum of light. The interaction of OAM beams with chiral molecules is naturally described by the minimal coupling Hamiltonian in which the transition moments are given as a spatial overlap integral that takes the following form: $\int d\mathbf{r} \mathbf{j}(\mathbf{r}) \cdot \mathbf{A}(\mathbf{r})e^{iL\varphi}$, where L is an integer representing the OAM, \mathbf{A} is the vector potential of the incoming X-ray beam, and \mathbf{j} is the transition current density operator. An alternative description in terms of multipole moments exists as well (123). Since the coupling appears as an overlap integral, the coupling between the light OAM and the molecular chirality is most efficient when the sizes are comparable. This constraint has so far hindered the efficient use of these beams for chiral spectroscopies in the optical domain. Because the diffraction limit scales with the wavelength, X-ray pulses allow one to achieve OAM at a focus size closer to molecular scales. Dichroic signals relying on the difference in absorption between $+L$ and $-L$ OAM beams have been demonstrated (124, 125) and named helical dichroism. Time-resolved versions of detection modes relying on OAM beams have not been well explored to date. Recent developments have demonstrated the ability of these beams to probe molecular coherences in diffraction signals, whether the probed molecule is chiral or not.

The chiral-sensitive signals covered in this section can be classified according to their coupling with matter: whether it is best described using the multipolar, the electric dipole, or the minimal coupling Hamiltonian. **Table 1** summarizes these XUV and X-ray signals.

4. COVARIANCE SIGNALS WITH STOCHASTIC X-RAY FREE-ELECTRON LASERS

Seeded free-electron lasers (FELs) at XUV photon energies offer stable coherent pulses (2) with the possibility of pulse shaping (126) and control (127). However, at higher photon energies, soft and hard XFELs based on the SASE mechanism (128) generate stochastic pulses with no phase control, resulting in noisy temporal and spectral profiles. This chaotic nature of X-ray SASE FEL pulses constitutes a major bottleneck for the implementation of multidimensional nonlinear X-ray spectroscopy protocols (129–131) such as TRUECARS, which require stable phase-controlled pulses and high joint temporal and spectral resolutions. Seeding protocols have been implemented to improve the coherence of hard-X-ray FEL pulses (132). High-intensity few-femtosecond pulses (133) with reduced-intensity spikes (134) have been demonstrated. However, because of their underlying SASE structure, these pulses are not reproducible from shot to shot.

Signals such as TRUECARS are sensitive to the pulse phase. The random variations in the phase of stochastic FEL pulses are imprinted into the signal, which thus vanishes upon averaging. Several theoretical and experimental studies are currently exploring protocols to circumvent this issue. A very promising approach takes advantage of machine learning to extract coherence information from chaotic data sets, as recently demonstrated for photoactive yellow protein undergoing a rapid *trans*-to-*cis* isomerization reaction via a CoIn (93). Here, we focus on covariance techniques, in which suitable products of observables are averaged over independent measurements in order to retrieve spectroscopic information. Covariance methods have been investigated in recent theoretical and experimental studies with stochastic optical lasers (135–137) and XFEL pulses (138–142). Below, we discuss how these correlation techniques, implemented with stochastic FEL pulses, can enable TRUECARS (51) and frequency-resolved TXRD (55) with existing FEL technology, without requiring either a broadband–narrowband hybrid pulse or control over the pulse phase.

Since each signal is uniquely related to the particular pulse producing it, spectroscopic information can be retrieved by analyzing at the data processing stage the correlation between the signal $S(\omega_{s2}, T)$, induced by a given stochastic pulse $\tilde{\mathcal{E}}(\omega)$, and the spectral intensity $|\tilde{\mathcal{E}}(\omega_{s1})|^2$ of that same pulse:

$$C(\omega_{s1}, \omega_{s2}, T) = \langle |\tilde{\mathcal{E}}(\omega_{s1})|^2 S(\omega_{s2}, T) \rangle - \langle |\tilde{\mathcal{E}}(\omega_{s1})|^2 \rangle \langle S(\omega_{s2}, T) \rangle, \quad 8.$$

where the angular brackets indicate an average over independent measurements. In Equation 8, the signals and the pulse spectral intensities are correlated at different frequencies, ω_{s2} and ω_{s1} , respectively; the frequency difference ($\omega_{s2} - \omega_{s1}$) here plays the role of the Raman frequency. The frequency ω_{s1} thus provides the reference necessary to reveal the Raman resonances in the molecule and the evolution of their time-dependent frequencies by scanning ω_{s2} .

For second-order signals such as TRUECARS, which involve two interactions with the probe pulse, Equation 8 is determined entirely by the two- and four-point field correlation functions, $F_2(\omega_1, \omega_2) \doteq \langle \tilde{\mathcal{E}}^*(\omega_1) \tilde{\mathcal{E}}(\omega_2) \rangle$ and $F_4(\omega_1, \omega_2, \omega_3, \omega_4) \doteq \langle \tilde{\mathcal{E}}^*(\omega_1) \tilde{\mathcal{E}}(\omega_2) \tilde{\mathcal{E}}^*(\omega_3) \tilde{\mathcal{E}}(\omega_4) \rangle$. By knowing these field correlation functions for stochastic FEL pulses, one can predict the properties of $C(\omega_{s1}, \omega_{s2}, T)$ and retrieve spectroscopic information. Suitable methods have long been utilized to model experiments with stochastic XFEL pulses (143–148) and simulate chaotic pulses with the correct statistical properties. **Figure 7a,b** depicts simulated temporal and spectral profiles of stochastic FEL pulses based on the model in References 51, 144, and 145, along with their average intensity profiles. This model was used (51) to predict the two- and four-point correlation functions of stochastic FEL pulses as well as to investigate TRUECARS and frequency-resolved TXRD, as discussed below.

4.1. TRUECARS

In the traditional TRUECARS setup with phase-controlled pulses, a hybrid broadband–narrowband probe is necessary in order to achieve joint high temporal and spectral resolutions. The duration and bandwidth of a coherent pulse are linked by Fourier uncertainty. Therefore, a large observation bandwidth and a controllable time–frequency resolution cannot be achieved by a single coherent pulse. However, stochastic FEL pulses feature chaotic temporal and spectral profiles, and their duration and spectral bandwidths are not linked by Fourier uncertainty. The same stochastic FEL pulse can, in principle, ensure a large observation bandwidth and a controllable time–frequency resolution, provided that spectroscopic information can be retrieved from chaotic signals. We therefore consider an implementation of TRUECARS involving a single stochastic FEL pulse interacting twice with the molecule. Given the TRUECARS signal in Equation 2, the

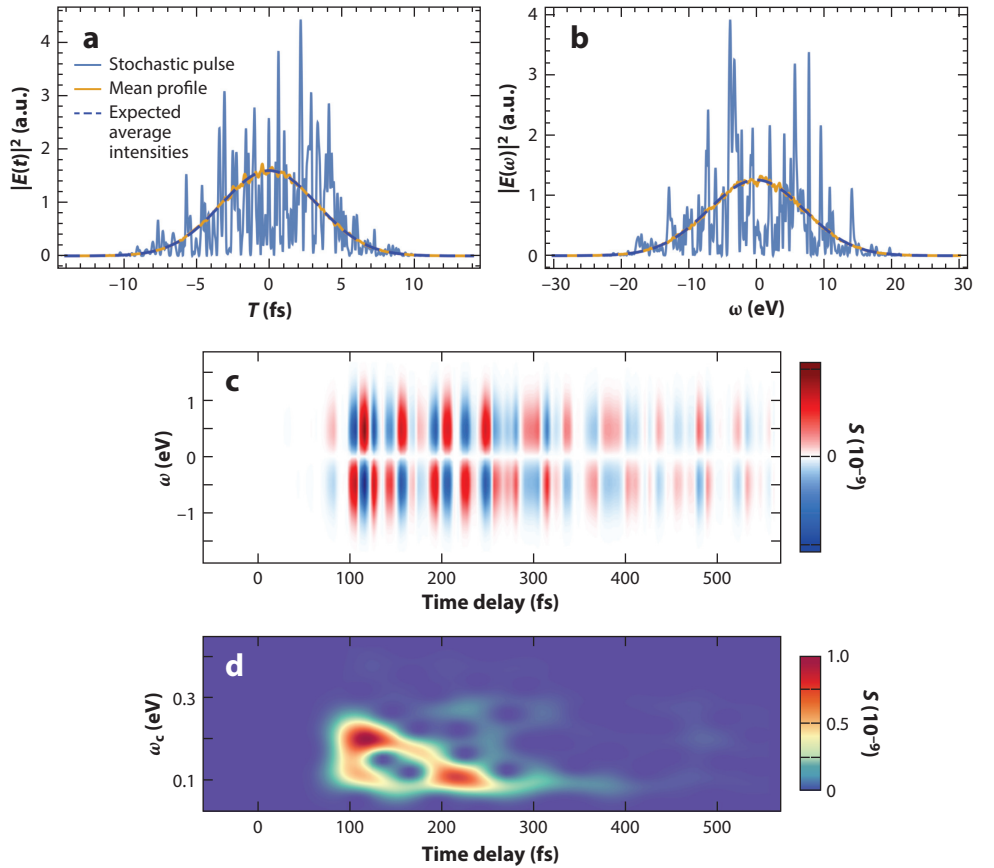


Figure 7

Simulated intensity profiles of a stochastic pulse based on the model presented in References 51, 144, and 145. The pulse has an average duration $\tau = 4.65$ fs ($1/\tau = 0.14$ eV) and bandwidth $\sigma = 10$ eV. (a) Temporal and (b) spectral intensity profiles. The solid blue curves represent one realization of the stochastic pulse; the solid yellow curves exhibit the mean profiles, obtained by averaging over 1,000 independent realizations. The dashed blue curves show the expected average intensities, calculated on the basis of the two-point correlation function of the model. (c) Simulated TRUECAR signal and (d) simulated spectrogram of uracil photorelaxation recorded with stochastic XFELs in a covariance approach. The coherent information is completely recovered, as evident via comparison with the signal in **Figure 3**. Abbreviations: TRUECARs, transient redistribution of ultrafast electronic coherences in attosecond Raman signals; XFEL, X-ray free-electron laser. Panels *a* and *b* adapted from Reference 51.

associated correlation function reduces to (51)

$$C(\omega_{s1}, \omega_{s2}, T) = 2 \operatorname{Im} \left\{ \int \frac{d\omega}{2\pi} \mathcal{G}(\omega_{s1}, \omega_{s2}, \omega) e^{-i\omega T} \langle \hat{\alpha}(\omega) \rangle \right\}, \quad 9.$$

with $\mathcal{G}(\omega_{s1}, \omega_{s2}, \omega) = F_4(\omega_{s1}, \omega_{s1}, \omega_{s2}, \omega_{s2} - \omega) - F_2(\omega_{s1}, \omega_{s1})F_2(\omega_{s2}, \omega_{s2} - \omega)$. The correlation properties of the stochastic FEL pulses thus determine the observation width and the time–frequency resolution of the technique. Reference 51 showed that a composite stochastic pulse, consisting of a short peaked pulse and a long broadband stochastic FEL pulse, can provide the favorable combination of parameters needed to enable large observation widths and time–frequency resolutions, without requiring any shaping or control of the pulse phase. The broad

frequency envelope of the stochastic pulse sets the observation bandwidth in a way analogous to $\tilde{\mathcal{E}}_{\text{B}}(\omega_s)$ for TRUECARS with a hybrid coherent probe. The pulse's overall time envelope instead determines the time–frequency resolution of the technique. It acts as a gate function on the evolution of the molecular polarization, playing a role completely analogous to $\mathcal{E}_{\text{N}}(t)$ for TRUECARS with a hybrid coherent probe. The detail of physical information accessed by TRUECARS implemented with a covariance analysis of stochastic signals is thus virtually identical to that obtained by phase-controlled pulses, as exemplified by Reference 51 for uracil nonadiabatic dynamics via a CoIn (compare **Figure 7c,d** with **Figure 3a,b**).

4.2. Frequency- and Time-Resolved X-Ray Diffraction

As discussed in Section 2.2, most X-ray photons contributing to the TXRD signal are scattered elastically off the electronic-state densities, with contributions from all electrons in the molecule. This elastic scattering represents a challenge when monitoring CoIns, where most core and valence electrons are inactive and only a few valence electrons are directly involved. Key temporal and spatial information about CoIn dynamics is encoded in the additional TXRD inelastic patterns (52, 53, 149) that stem from the localized quantum coherences generated at CoIns. These signatures are scattered off transition charge densities, which map the few electrons involved in the CoIn passage without background contributions from the remaining inactive ones.

Frequency-dispersed TXRD signals could provide a means to spectrally separate the elastic (population) and the inelastic (coherence) contributions and follow their evolution in time. In a TXRD setup, this could be achieved by detecting the X-rays scattered off the sample by an array of frequency spectrometers, which disperse the spontaneously emitted photons in momentum \mathbf{k} , and frequency ω_s (150). However, existing stochastic broadband FEL pulses generate ensembles of stochastic signals that, upon averaging, do not provide the spectral resolution required for an effective separation of elastic and inelastic scattering contributions.

Also, for frequency-dispersed TXRD, as discussed above for TRUECARS, this limitation of stochastic FEL pulses can be circumvented by a covariance approach (55). One can introduce the correlation function of Equation 8, where S now denotes the momentum-, frequency-, and time-resolved X-ray diffraction signal $S(\mathbf{q}, \omega_s, T)$, and average this correlation function over independent measurements. For frequency-resolved TXRD, the signal involves two interactions with the stochastic pulse, and the correlation function is thus determined by the two- and four-point correlation function of the field. We note that TXRD is a spontaneous technique where the pulse properties determine the time–frequency resolution but do not affect the spectral observation width of the signal. In contrast, TRUECARS is a stimulated heterodyne detection scheme where the pulse bandwidth determines the spectral observation width of the technique.

Reference 55 exemplifies a covariance approach for frequency-dispersed TXRD for powder diffraction off randomly oriented nanocrystals of azobenzene molecules undergoing photoisomerization through a CoIn (53). The correlation signal allows one to monitor the molecular coherences that emerge during the nonadiabatic dynamics, revealing a confined distribution of transition charge densities representing small distances in the molecule. Implemented in a crystal, covariance TXRD could offer background-free, fully three-dimensional reconstruction of transition charge densities at CoIns.

5. CONCLUSIONS

The techniques surveyed above address a primary chemical event—passage through CoIns—from different angles. They are enabled by novel ultrafast X-ray and electron sources from FELs and tabletop setups. The signals are based on vibronic coherences that emerge due to the bifurcation

of nuclear wave packets at points of electronic degeneracy, and provide more direct probes of non-adiabatic passages in comparison to, for instance, observing abrupt shifts in transient absorption lines stemming from populations. In TRUECARS, the populations do not even contribute, and the vibronic coherences can be detected free from the usually dominating background. Still, large enough cross sections must be achieved experimentally to compete with loss channels, such as ionization and Auger–Meitner decay. These cross sections can be enhanced by preresonant tuning of the X-ray pulse energy (51) or by employing quantum optimal control strategies to enhance the coherence magnitude (54, 151). Through its spectrogram, TRUECARS provides information about the energy splitting of the adiabatic states and the underlying vibronic coherences (49).

TXRD is a scattering-based technique that provides spatial information not accessible with TRUECARS or tr-PES. The coherences are masked by much stronger contributions and are therefore hard to detect, but their relative strength can be increased by recording larger momentum transfer amplitudes using hard X-rays (53). They exhibit oscillations that correspond to the phase change of the electronic transition density, as the molecule traverses the CoIn. UED provides additional information by scattering from nuclear charge densities, which contain mixed nuclear + electronic contributions. Heterodyned TXRD and UED could even be combined to accomplish exclusive sensitivity to nuclear wave packets (100). This is a very difficult experimental challenge that could give rise to a new family of signatures not available via any other technique.

tr-PES, a well-established technique for the study of nonadiabatic molecular dynamics, contains contributions from vibronic coherences at CoIns. Again, they are much weaker than the population signatures that tr-PES studies usually focus on, but in principle they could be detected and separated out via transient gating operations at the postprocessing stage.

Molecular chirality is another interesting chemical phenomenon in which X-ray and HHG sources can drastically increase the probing capabilities. We have discussed various signals that offer novel ways to access chiral molecular information. Chiral dynamics, if triggered in the excited state, is inherently linked to CoIns that open and connect the photoproduct pathways. In the future, it will be an interesting challenge to connect chirality-sensitive signals to CoIns and explore how nonadiabatic passages influence the enantiomeric yield of chiral molecular dynamics.

Section 4 has discussed how to overcome a major obstacle in the practical implementation of the proposed techniques: the stochastic nature of SASE-generated FEL pulses. By measuring the spectrum in coincidence with the probe pulse generating it, and averaging over many individual realizations, one can overcome the absence of phase control and recover coherent information obtained by the techniques discussed above. This can be crucial for experimentally realizing the theoretical proposals with current pulse technology, although other difficulties still make these measurements very challenging. Altogether, these techniques can provide unique insights into elementary molecular events. Connecting a new family of properties to the efficiency of CoIns could lead to novel design opportunities for molecules and materials that rely on CoIns as their operational principle—including, for example, molecular switches and motors.

DISCLOSURE STATEMENT

The authors are not aware of any affiliations, memberships, funding, or financial holdings that might be perceived as affecting the objectivity of this review.

ACKNOWLEDGMENTS

S.M. is a fellow of the Hagler Institute for Advanced Study at Texas A&M University. We thank our long-time collaborators Sergei Tretiak and Niri Govind for their most valuable contributions to this research. The work covered in this review was supported by the Chemical Sciences,

Geosciences, and Biosciences Division, Office of Basic Energy Sciences, Office of Science, US Department of Energy, through awards DE-SC0022225 and DE-FG02-04ER15571 (to S.M.C., H.Y., and J.R.R.), and by the National Science Foundation under award number CHE-1953045. D.K. and S.M.C. gratefully acknowledge support from the Alexander von Humboldt Foundation through the Feodor Lynen Research Fellowship.

LITERATURE CITED

1. Emma P, Akre R, Arthur J, Bionta R, Bostedt C, et al. 2010. First lasing and operation of an ångström-wavelength free-electron laser. *Nat. Photon.* 4(9):641–47
2. Allaria E, Appio R, Badano L, Barletta W, Bassanese S, et al. 2012. Highly coherent and stable pulses from the FERMI seeded free-electron laser in the extreme ultraviolet. *Nat. Photon.* 6(10):699–704
3. Tono K, Togashi T, Inubushi Y, Sato T, Katayama T, et al. 2013. Beamline, experimental stations and photon beam diagnostics for the hard X-ray free electron laser of SACLA. *New J. Phys.* 15:083035
4. Milne C, Schietinger T, Aiba M, Alarcon A, Alex J, et al. 2017. SwissFEL: the Swiss X-ray Free Electron Laser. *Appl. Sci.* 7(7):720
5. Abeghyan S, Bagha-Shanjani M, Chen G, Englisch U, Karabekyan S, et al. 2019. First operation of the SASE1 undulator system of the European X-ray Free-Electron Laser. *J. Synchrotron Radiat.* 26(2):302–10
6. Yang H, Kim G, Kang HS. 2018. First saturation of 14.5 keV free electron laser at PAL-XFEL. *Nucl. Instrum. Methods A* 911:51–54
7. Zhang B, Yu Y, Zhang Z, Zhang YY, Jiang S, et al. 2020. Infrared spectroscopy of neutral water dimer based on a tunable vacuum ultraviolet free electron laser. *J. Phys. Chem. Lett.* 11(3):851–55
8. Young L, Ueda K, Gühr M, Bucksbaum PH, Simon M, et al. 2018. Roadmap of ultrafast X-ray atomic and molecular physics. *J. Phys. B* 51:032003
9. Duris J, Li S, Driver T, Champenois EG, MacArthur JP, et al. 2020. Tunable isolated attosecond X-ray pulses with gigawatt peak power from a free-electron laser. *Nat. Photon.* 14(1):30–36
10. Emma P, Bane K, Cornacchia M, Huang Z, Schlarb H, et al. 2004. Femtosecond and subfemtosecond X-ray pulses from a self-amplified spontaneous-emission-based free-electron laser. *Phys. Rev. Lett.* 92:074801
11. Saa Hernandez A, Prat E, Bettoni S, Beutner B, Reiche S. 2016. Generation of large-bandwidth X-ray free-electron-laser pulses. *Phys. Rev. Accel. Beams* 19:090702
12. Prat E, Calvi M, Reiche S. 2016. Generation of ultra-large-bandwidth X-ray free-electron-laser pulses with a transverse-gradient undulator. *J. Synchrotron Radiat.* 23(4):874–79
13. Inoue I, Osaka T, Hara T, Tanaka T, Inagaki T, et al. 2019. Generation of narrow-band X-ray free-electron laser via reflection self-seeding. *Nat. Photon.* 13(5):319–22
14. Amini K, Biegert J, Calegari F, Chacón A, Ciappina MF, et al. 2019. Symphony on strong field approximation. *Rep. Prog. Phys.* 82:116001
15. Li J, Ren X, Yin Y, Zhao K, Chew A, et al. 2017. 53-attosecond X-ray pulses reach the carbon K-edge. *Nat. Commun.* 8:186
16. Teichmann SM, Silva F, Cousin SL, Hemmer M, Biegert J. 2016. 0.5-keV soft X-ray attosecond continua. *Nat. Commun.* 7:11493
17. Cousin SL, Di Palo N, Buades B, Teichmann SM, Reduzzi M, et al. 2017. Attosecond streaking in the water window: a new regime of attosecond pulse characterization. *Phys. Rev. X* 7:041030
18. Kleine C, Ekimova M, Goldsztejn G, Raabe S, Strüber C, et al. 2019. Soft X-ray absorption spectroscopy of aqueous solutions using a table-top femtosecond soft X-ray source. *J. Phys. Chem. Lett.* 10(1):52–58
19. Worner HJ, Bertrand JB, Fabre B, Higuert J, Ruf H, et al. 2011. Conical intersection dynamics in NO₂ probed by homodyne high-harmonic spectroscopy. *Science* 334(6053):208–12
20. Chergui M, Collet E. 2017. Photoinduced structural dynamics of molecular systems mapped by time-resolved X-ray methods. *Chem. Rev.* 117(16):11025–65
21. Wolf TJA, Myhre RH, Cryan JP, Coriani S, Squibb RJ, et al. 2017. Probing ultrafast $\pi\pi^*/\pi\pi^*$ internal conversion in organic chromophores via K-edge resonant absorption. *Nat. Commun.* 8:29
22. Attar AR, Bhattacharjee A, Pemmaraju CD, Schnorr K, Closser KD, et al. 2017. Femtosecond X-ray spectroscopy of an electrocyclic ring-opening reaction. *Science* 356(6333):54–59

23. Pathak S, Ibele LM, Boll R, Callegari C, Demidovich A, et al. 2020. Tracking the ultraviolet-induced photochemistry of thiophenone during and after ultrafast ring opening. *Nat. Chem.* 12(9):795–800
24. Rebholz M, Ding T, Despré V, Aufleger L, Hartmann M, et al. 2021. All-XUV pump-probe transient absorption spectroscopy of the structural molecular dynamics of di-iodomethane. *Phys. Rev. X* 11:031001
25. Mayer D, Lever F, Picconi D, Metje J, Alisauskas S, et al. 2022. Following excited-state chemical shifts in molecular ultrafast X-ray photoelectron spectroscopy. *Nat. Commun.* 13:198
26. Minitti MP, Budarz JM, Kirrander A, Robinson JS, Ratner D, et al. 2015. Imaging molecular motion: femtosecond X-ray scattering of an electrocyclic chemical reaction. *Phys. Rev. Lett.* 114:255501
27. Stankus B, Yong H, Zotev N, Ruddock JM, Bellshaw D, et al. 2019. Ultrafast X-ray scattering reveals vibrational coherence following Rydberg excitation. *Nat. Chem.* 11(8):716–21
28. Kim JG, Nozawa S, Kim H, Choi EH, Sato T, et al. 2020. Mapping the emergence of molecular vibrations mediating bond formation. *Nature* 582(7813):520–24
29. Yong H, Zotev N, Ruddock JM, Stankus B, Simmermacher M, et al. 2020. Observation of the molecular response to light upon photoexcitation. *Nat. Commun.* 11:2157
30. Biasin E, Fox ZW, Andersen A, Ledbetter K, Kjær KS, et al. 2021. Direct observation of coherent femtosecond solvent reorganization coupled to intramolecular electron transfer. *Nat. Chem.* 13(4):343–49
31. Jahnke T, Guillemin R, Inhester L, Son SK, Kastirke G, et al. 2021. Inner-shell-ionization-induced femtosecond structural dynamics of water molecules imaged at an X-ray free-electron laser. *Phys. Rev. X* 11:041044
32. Boll R, Schäfer JM, Richard B, Fehre K, Kastirke G, et al. 2022. X-ray multiphoton-induced Coulomb explosion images complex single molecules. *Nat. Phys.* 18(4):423–28
33. Pandey S, Bean R, Sato T, Poudyal I, Bielecki J, et al. 2020. Time-resolved serial femtosecond crystallography at the European XFEL. *Nat. Methods* 17(1):73–78
34. Brändén G, Neutze R. 2021. Advances and challenges in time-resolved macromolecular crystallography. *Science* 373(6558):aba0954
35. Suzuki T. 2021. Spiers Memorial Lecture: introduction to ultrafast spectroscopy and imaging of photochemical reactions. *Faraday Discuss.* 228:11–38
36. Ivanov M. 2021. The age of molecular movies. *Faraday Discuss.* 228:622–29
37. Calegari F, Ayuso D, Trabattoni A, Belshaw L, De Camillis S, et al. 2014. Ultrafast electron dynamics in phenylalanine initiated by attosecond pulses. *Science* 346(6207):336–39
38. Kraus PM, Mignolet B, Baykusheva D, Rupenyana A, Horný L, et al. 2015. Measurement and laser control of attosecond charge migration in ionized iodoacetylene. *Science* 350(6262):790–95
39. Li S, Driver T, Rosenberger P, Champenois EG, Duris J, et al. 2022. Attosecond coherent electron motion in Auger–Meitner decay. *Science* 375(6578):285–90
40. Domcke W, Yarkony DR, Köppel H. 2011. *Conical Intersections*. Singapore: World Sci.
41. Farag MH, Jansen TLC, Knoester J. 2016. Probing the interstate coupling near a conical intersection by optical spectroscopy. *J. Phys. Chem. Lett.* 7(17):3328–34
42. Polli D, Altoè P, Weingart O, Spillane KM, Manzoni C, et al. 2010. Conical intersection dynamics of the primary photoisomerization event in vision. *Nature* 467(7314):440–43
43. Lim JS, Kim SK. 2010. Experimental probing of conical intersection dynamics in the photodissociation of thioanisole. *Nat. Chem.* 2(8):627–32
44. Hartmann N, Hartmann G, Heider R, Wagner MS, Ilchen M, et al. 2018. Attosecond time-energy structure of X-ray free-electron laser pulses. *Nat. Photon.* 12(4):215–20
45. Prat E, Reiche S. 2015. Simple method to generate terawatt-attosecond X-ray free-electron-laser pulses. *Phys. Rev. Lett.* 114:244801
46. Kobayashi Y, Chang KF, Zeng T, Neumark DM, Leone SR. 2019. Direct mapping of curve-crossing dynamics in IBr by attosecond transient absorption spectroscopy. *Science* 364(6448):79–83
47. Zinchenko KS, Ardana-Lamas F, Seidu I, Neville SP, van der Veen J, et al. 2021. Sub-7-femtosecond conical-intersection dynamics probed at the carbon K-edge. *Science* 371(6528):489–94
48. Kowalewski M, Bennett K, Dorfman KE, Mukamel S. 2015. Catching conical intersections in the act: monitoring transient electronic coherences by attosecond stimulated X-ray Raman signals. *Phys. Rev. Lett.* 115:193003

49. Keefer D, Schnappinger T, de Vivie-Riedle R, Mukamel S. 2020. Visualizing conical intersection passages via vibronic coherence maps generated by stimulated ultrafast X-ray Raman signals. *PNAS* 117(39):24069–75
50. Keefer D, Freixas VM, Song H, Tretiak S, Fernandez-Alberti S, Mukamel S. 2021. Monitoring molecular vibronic coherences in a bichromophoric molecule by ultrafast X-ray spectroscopy. *Chem. Sci.* 12(14):5286–94
51. Cavaletto SM, Keefer D, Mukamel S. 2021. High temporal and spectral resolution of stimulated X-ray Raman signals with stochastic free-electron-laser pulses. *Phys. Rev. X* 11:011029
52. Bennett K, Kowalewski M, Rouxel JR, Mukamel S. 2018. Monitoring molecular nonadiabatic dynamics with femtosecond X-ray diffraction. *PNAS* 115(26):6538–47
53. Keefer D, Aleotti F, Rouxel JR, Segatta F, Gu B, et al. 2021. Imaging conical intersection dynamics during azobenzene photoisomerization by ultrafast X-ray diffraction. *PNAS* 118(3):e2022037118
54. Keefer D, Rouxel JR, Aleotti F, Segatta F, Garavelli M, Mukamel S. 2021. Diffractive imaging of conical intersections amplified by resonant infrared fields. *J. Am. Chem. Soc.* 143(34):13806–15
55. Cavaletto SM, Keefer D, Rouxel JR, Aleotti F, Segatta F, et al. 2021. Unveiling the spatial distribution of molecular coherences at conical intersections by covariance X-ray diffraction signals. *PNAS* 118(22):e2105046118
56. Rouxel JR, Keefer D, Mukamel S. 2021. Signatures of electronic and nuclear coherences in ultrafast molecular X-ray and electron diffraction. *Struct. Dyn.* 8:014101
57. Rouxel JR, Keefer D, Aleotti F, Nenov A, Garavelli M, Mukamel S. 2022. Coupled electronic and nuclear motions during azobenzene photoisomerization monitored by ultrafast electron diffraction. *J. Chem. Theory Comput.* 18(2):605–13
58. Bennett K, Kowalewski M, Mukamel S. 2016. Nonadiabatic dynamics may be probed through electronic coherence in time-resolved photoelectron spectroscopy. *J. Chem. Theory Comput.* 12(2):740–52
59. Cavaletto SM, Keefer D, Mukamel S. 2022. Electronic coherences in nonadiabatic molecular photophysics revealed by time-resolved photoelectron spectroscopy. *PNAS* 119(11):e2121383119
60. Hüll K, Morstein J, Trauner D. 2018. In vivo photopharmacology. *Chem. Rev.* 118(21):10710–47
61. Goulet-Hanssens A, Eisenreich F, Hecht S. 2020. Enlightening materials with photoswitches. *Adv. Mater.* 32(20):1905966
62. Reiter S, Keefer D, de Vivie-Riedle R. 2020. Exact quantum dynamics (wave packets) in reduced dimensionality. In *Quantum Chemistry and Dynamics of Excited States*, ed. L. González, R Lindh, pp. 355–81. New York: Wiley
63. Tully JC. 1990. Molecular dynamics with electronic transitions. *J. Chem. Phys.* 93(2):1061–71
64. Richter M, Marquetand P, González-Vázquez J, Sola I, González L. 2011. SHARC: ab initio molecular dynamics with surface hopping in the adiabatic representation including arbitrary couplings. *J. Chem. Theory Comput.* 7(5):1253–58
65. Ben-Nun M, Quenneville J, Martínez TJ. 2000. Ab initio multiple spawning: photochemistry from first principles quantum molecular dynamics. *J. Phys. Chem. A* 104(22):5161–75
66. Makhov DV, Glover WJ, Martínez TJ, Shalashilin DV. 2014. Ab initio multiple cloning algorithm for quantum nonadiabatic molecular dynamics. *J. Chem. Phys.* 141:054110
67. Meyer HD, Manthe U, Cederbaum L. 1990. The multi-configurational time-dependent Hartree approach. *Chem. Phys. Lett.* 165(1):73–78
68. Kowalewski M, Fingerhut BP, Dorfman KE, Bennett K, Mukamel S. 2017. Simulating coherent multi-dimensional spectroscopy of nonadiabatic molecular processes: from the infrared to the X-ray regime. *Chem. Rev.* 117(19):12165–226
69. Restaino L, Jadoun D, Kowalewski M. 2022. Probing nonadiabatic dynamics with attosecond pulse trains and soft X-ray Raman spectroscopy. *Struct. Dyn.* 9:034101
70. Cho D, Rouxel JR, Mukamel S. 2020. Stimulated X-ray resonant Raman spectroscopy of conical intersections in thiophenol. *J. Phys. Chem. Lett.* 11(11):4292–97
71. Segatta F, Nenov A, Orlandi A, Arcioni A, Mukamel S, Garavelli M. 2020. Exploring the capabilities of optical pump X-ray probe NEXAFS spectroscopy to track photo-induced dynamics mediated by conical intersections. *Faraday Discuss.* 221:245–64

72. Chang KF, Reduzzi M, Wang H, Poullain SM, Kobayashi Y, et al. 2020. Revealing electronic state-switching at conical intersections in alkyl iodides by ultrafast XUV transient absorption spectroscopy. *Nat. Commun.* 11:4042
73. Trebino R, DeLong KW, Fittinghoff DN, Sweetser JN, Krumbügel MA, et al. 1997. Measuring ultrashort laser pulses in the time-frequency domain using frequency-resolved optical gating. *Rev. Sci. Instrum.* 68(9):3277–95
74. Linden S, Giessen H, Kuhl J. 1998. XFROG—a new method for amplitude and phase characterization of weak ultrashort pulses. *Phys. Status Solidi B* 206(1):119–24
75. Nam Y, Keefer D, Nenov A, Conti I, Aleotti F, et al. 2021. Conical intersection passages of molecules probed by X-ray diffraction and stimulated Raman spectroscopy. *J. Phys. Chem. Lett.* 12(51):12300–9
76. Gu B, Keefer D, Aleotti F, Nenov A, Garavelli M, Mukamel S. 2021. Photoisomerization transition state manipulation by entangled two-photon absorption. *PNAS* 118(47):e2116868118
77. Freixas VM, Keefer D, Tretiak S, Fernandez-Alberti S, Mukamel S. 2022. Ultrafast coherent photoexcited dynamics in a trimeric dendrimer probed by X-ray stimulated-Raman signals. *Chem. Sci.* 13:6373–84
78. Wituschek A, Bruder L, Allaria E, Bangert U, Binz M, et al. 2020. Tracking attosecond electronic coherences using phase-manipulated extreme ultraviolet pulses. *Nat. Commun.* 11:883
79. Spence JCH. 2017. Outrunning damage: electrons versus X-rays—timescales and mechanisms. *Struct. Dyn.* 4:044027
80. Stefanou M, Saita K, Shalashilin DV, Kirrander A. 2017. Comparison of ultrafast electron and X-ray diffraction—a computational study. *Chem. Phys. Lett.* 683:300–5
81. Ma L, Yong H, Geiser JD, Moreno Carrascosa A, Goff N, Weber PM. 2020. Ultrafast X-ray and electron scattering of free molecules: a comparative evaluation. *Struct. Dyn.* 7:034102
82. Thakkar AJ, Tripathi AN, Smith VH. 1984. Molecular X-ray- and electron-scattering intensities. *Phys. Rev. A* 29(3):1108–13
83. Warren BE. 1969. *X-Ray Diffraction*. Reading, MA: Addison-Wesley
84. Hofstadter R. 1956. Electron scattering and nuclear structure. *Rev. Mod. Phys.* 28(3):214–54
85. Chapman HN, Fromme P, Barty A, White TA, Kirian RA, et al. 2011. Femtosecond X-ray protein nanocrystallography. *Nature* 470(7332):73–77
86. Decking W, Abeghyan S, Abramian P, Abramsky A, Aguirre A, et al. 2020. A MHz-repetition-rate hard X-ray free-electron laser driven by a superconducting linear accelerator. *Nat. Photon.* 14(6):391–97
87. Weathersby SP, Brown G, Centurion M, Chase TF, Coffee R, et al. 2015. Mega-electron-volt ultrafast electron diffraction at SLAC National Accelerator Laboratory. *Rev. Sci. Instrum.* 86:073702
88. Qi F, Ma Z, Zhao L, Cheng Y, Jiang W, et al. 2020. Breaking 50 femtosecond resolution barrier in MeV ultrafast electron diffraction with a double bend achromat compressor. *Phys. Rev. Lett.* 124:134803
89. Wolf TJA, Sanchez DM, Yang J, Parrish RM, Nunes JPF, et al. 2019. The photochemical ring-opening of 1,3-cyclohexadiene imaged by ultrafast electron diffraction. *Nat. Chem.* 11(6):504–9
90. Ruddock JM, Yong H, Stankus B, Du W, Goff N, et al. 2019. A deep UV trigger for ground-state ring-opening dynamics of 1,3-cyclohexadiene. *Sci. Adv.* 5(9):aax6625
91. Yang J, Zhu X, Wolf TJA, Li Z, Nunes JPF, et al. 2018. Imaging CF₃I conical intersection and photodissociation dynamics with ultrafast electron diffraction. *Science* 361(6397):64–67
92. Ruddock JM, Zotev N, Stankus B, Yong H, Bellshaw D, et al. 2019. Simplicity beneath complexity: Counting molecular electrons reveals transients and kinetics of photodissociation reactions. *Angew. Chem. Int. Ed.* 58(19):6371–75
93. Hosseinizadeh A, Breckwoldt N, Fung R, Sepehr R, Schmidt M, et al. 2021. Few-fs resolution of a photoactive protein traversing a conical intersection. *Nature* 599(7886):697–701
94. Henriksen NE, Møller KB. 2008. On the theory of time-resolved X-ray diffraction. *J. Phys. Chem. B* 112(2):558–67
95. Dixit G, Vendrell O, Santra R. 2012. Imaging electronic quantum motion with light. *PNAS* 109(29):11636–40
96. Kowalewski M, Bennett K, Mukamel S. 2017. Monitoring nonadiabatic avoided crossing dynamics in molecules by ultrafast X-ray diffraction. *Struct. Dyn.* 4:054101

97. Simmermacher M, Moreno Carrascosa A, Henriksen NE, Møller KB, Kirrander A. 2019. Theory of ultrafast X-ray scattering by molecules in the gas phase. *J. Chem. Phys.* 151:174302
98. Rouxel JR, Keefer D, Aleotti F, Nenov A, Garavelli M, Mukamel S. 2022. Coupled electronic and nuclear motions during azobenzene photoisomerization monitored by ultrafast electron diffraction. *J. Chem. Theory Comput.* 18(2):605–13
99. Yang J, Zhu X, Nunes JPF, Yu JK, Parrish RM, et al. 2020. Simultaneous observation of nuclear and electronic dynamics by ultrafast electron diffraction. *Science* 368(6493):885–89
100. Yong H, Keefer D, Mukamel S. 2022. Imaging purely nuclear quantum dynamics in molecules by combined X-ray and electron diffraction. *J. Am. Chem. Soc.* 144(17):7796–804
101. Carlson TA. 1975. Photoelectron spectroscopy. *Annu. Rev. Phys. Chem.* 26:211–34
102. Neumark DM. 2001. Time-resolved photoelectron spectroscopy of molecules and clusters. *Annu. Rev. Phys. Chem.* 52:255–77
103. Stolow A, Bragg AE, Neumark DM. 2004. Femtosecond time-resolved photoelectron spectroscopy. *Chem. Rev.* 104(4):1719–58
104. Wollenhaupt M, Engel V, Baumert T. 2005. Femtosecond laser photoelectron spectroscopy on atoms and small molecules: prototype studies in quantum control. *Annu. Rev. Phys. Chem.* 56:25–56
105. von Conta A, Tehlar A, Schletter A, Arasaki Y, Takatsuka K, Wörner HJ. 2018. Conical-intersection dynamics and ground-state chemistry probed by extreme-ultraviolet time-resolved photoelectron spectroscopy. *Nat. Commun.* 9:3162
106. Wolf TJA, Parrish RM, Myhre RH, Martínez TJ, Koch H, Gühr M. 2019. Observation of ultrafast intersystem crossing in thymine by extreme ultraviolet time-resolved photoelectron spectroscopy. *J. Phys. Chem. A* 123(32):6897–903
107. Brauße F, Goldsztejn G, Amini K, Boll R, Bari S, et al. 2018. Time-resolved inner-shell photoelectron spectroscopy: from a bound molecule to an isolated atom. *Phys. Rev. A* 97:043429
108. Hudock HR, Levine BG, Thompson AL, Satzger H, Townsend D, et al. 2007. Ab initio molecular dynamics and time-resolved photoelectron spectroscopy of electronically excited uracil and thymine. *J. Phys. Chem. A* 111(34):8500–8
109. Glover WJ, Mori T, Schuurman MS, Boguslavskiy AE, Schalk O, et al. 2018. Excited state non-adiabatic dynamics of the smallest polyene, *trans* 1,3-butadiene. II. *Ab initio* multiple spawning simulations. *J. Chem. Phys.* 148:164303
110. Chakraborty P, Liu Y, McClung S, Weinacht T, Matsika S. 2021. Time resolved photoelectron spectroscopy as a test of electronic structure and nonadiabatic dynamics. *J. Phys. Chem. Lett.* 12(21):5099–104
111. Makhija V, Veyrinas K, Boguslavskiy AE, Forbes R, Wilkinson I, et al. 2020. Ultrafast molecular frame electronic coherences from lab frame scattering anisotropies. *J. Phys. B* 53:114001
112. Jadoun D, Kowalewski M. 2021. Time-resolved photoelectron spectroscopy of conical intersections with attosecond pulse trains. *J. Phys. Chem. Lett.* 12(33):8103–8
113. Lutman AA, MacArthur JP, Ilchen M, Lindahl AO, Buck J, et al. 2016. Polarization control in an X-ray free-electron laser. *Nat. Photon.* 10(7):468–72
114. Hernández-García C, Durfee CG, Hickstein DD, Popmintchev T, Meier A, et al. 2016. Schemes for generation of isolated attosecond pulses of pure circular polarization. *Phys. Rev. A* 93:043855
115. Zhang Y, Rouxel JR, Autschbach J, Govind N, Mukamel S. 2017. X-ray circular dichroism signals: a unique probe of local molecular chirality. *Chem. Sci.* 8(9):5969–78
116. Mincigrucci R, Rouxel J, Rossi B, Principi E, Bottari C, et al. 2020. Element- and enantiomer-selective visualization of ibuprofen dimer vibrations. arXiv:2010.04860 [cond-mat.soft]
117. Rouxel JR, Kowalewski M, Mukamel S. 2017. Photoinduced molecular chirality probed by ultrafast resonant X-ray spectroscopy. *Struct. Dyn.* 4:044006
118. Weingart O, Lan Z, Koslowski A, Thiel W. 2011. Chiral pathways and periodic decay in *cis*-azobenzene photodynamics. *J. Phys. Chem. Lett.* 2(13):1506–9
119. Ordóñez AF, Smirnova O. 2018. Generalized perspective on chiral measurements without magnetic interactions. *Phys. Rev. A* 98:063428
120. Beaulieu S, Comby A, Fabre B, Descamps D, Ferré A, et al. 2016. Probing ultrafast dynamics of chiral molecules using time-resolved photoelectron circular dichroism. *Faraday Discuss.* 194:325–48

121. Cireasa R, Boguslavskiy AE, Pons B, Wong MCH, Descamps D, et al. 2015. Probing molecular chirality on a sub-femtosecond timescale. *Nat. Phys.* 11(8):654–58
122. Ye L, Rouxel JR, Asban S, Rösner B, Mukamel S. 2019. Probing molecular chirality by orbital-angular-momentum-carrying X-ray pulses. *J. Chem. Theory Comput.* 15(7):4180–86
123. Forbes KA, Andrews DL. 2018. Optical orbital angular momentum: twisted light and chirality. *Opt. Lett.* 43(3):435–38
124. Rouxel JR, Rosner B, Karpov D, Bacellar C, Mancini GF, et al. 2022. Hard X-ray helical dichroism of disordered molecular media. *Nat. Photon.* 16(8):570–74
125. Brullot W, Vanbel MK, Swusten T, Verbiest T. 2016. Resolving enantiomers using the optical angular momentum of twisted light. *Sci. Adv.* 2(3):e1501349
126. Gauthier D, Ribič PR, De Ninno G, Allaria E, Cinquegrana P, et al. 2015. Spectrotemporal shaping of seeded free-electron laser pulses. *Phys. Rev. Lett.* 115:114801
127. Prince KC, Allaria E, Callegari C, Cucini R, De Ninno G, et al. 2016. Coherent control with a short-wavelength free-electron laser. *Nat. Photon.* 10(3):176–79
128. Bonifacio R, Pellegrini C, Narducci L. 1984. Collective instabilities and high-gain regime in a free electron laser. *Opt. Commun.* 50(6):373–78
129. Biggs JD, Zhang Y, Healion D, Mukamel S. 2013. Watching energy transfer in metalloporphyrin heterodimers using stimulated X-ray Raman spectroscopy. *PNAS* 110(39):15597–601
130. Healion D, Zhang Y, Biggs JD, Govind N, Mukamel S. 2012. Entangled valence electron-hole dynamics revealed by stimulated attosecond X-ray Raman scattering. *J. Phys. Chem. Lett.* 3(17):2326–31
131. Zhang Y, Biggs JD, Govind N, Mukamel S. 2014. Monitoring long-range electron transfer pathways in proteins by stimulated attosecond broadband X-ray Raman spectroscopy. *J. Phys. Chem. Lett.* 5(21):3656–61
132. Amann J, Berg W, Blank V, Decker FJ, Ding Y, et al. 2012. Demonstration of self-seeding in a hard-X-ray free-electron laser. *Nat. Photon.* 6(10):693–98
133. Marinelli A, Ratner D, Lutman A, Turner J, Welch J, et al. 2015. High-intensity double-pulse X-ray free-electron laser. *Nat. Commun.* 6:6369
134. Lutman AA, Guetg MW, Maxwell TJ, MacArthur JP, Ding Y, et al. 2018. High-power femtosecond soft X rays from fresh-slice multistage free-electron lasers. *Phys. Rev. Lett.* 120:264801
135. Tollerud JO, Sparapassi G, Montanaro A, Asban S, Glerean F, et al. 2019. Femtosecond covariance spectroscopy. *PNAS* 116(12):5383–86
136. Osipov VA, Asban S, Mukamel S. 2019. Time and frequency resolved transient-absorption and stimulated-Raman signals of stochastic light. *J. Chem. Phys.* 151:044113
137. Sparapassi G, Cavaletto SM, Tollerud J, Montanaro A, Glerean F, et al. 2022. Transient measurement of phononic states with covariance-based stochastic spectroscopy. *Light Sci. Appl.* 11(1):44
138. Kimberg V, Rohringer N. 2016. Stochastic stimulated electronic X-ray Raman spectroscopy. *Struct. Dyn.* 3:034101
139. Gorobtsov OY, Mercurio G, Capotondi F, Skopintsev P, Lazarev S, et al. 2018. Seeded X-ray free-electron laser generating radiation with laser statistical properties. *Nat. Commun.* 9:4498
140. Asban S, Cho D, Mukamel S. 2019. Frequency-, time-, and wavevector-resolved ultrafast incoherent diffraction of noisy X-ray pulses. *J. Phys. Chem. Lett.* 10(19):5805–14
141. Kayser Y, Milne C, Juranić P, Sala L, Czaplá-Masztafiak J, et al. 2019. Core-level nonlinear spectroscopy triggered by stochastic X-ray pulses. *Nat. Commun.* 10:4761
142. Driver T, Li S, Champenois EG, Duris J, Ratner D, et al. 2020. Attosecond transient absorption spooktroscopy: a ghost imaging approach to ultrafast absorption spectroscopy. *Phys. Chem. Chem. Phys.* 22(5):2704–12
143. Rohringer N, Santra R. 2007. X-ray nonlinear optical processes using a self-amplified spontaneous emission free-electron laser. *Phys. Rev. A* 76:033416
144. Pfeifer T, Jiang Y, Düsterer S, Moshhammer R, Ullrich J. 2010. Partial-coherence method to model experimental free-electron laser pulse statistics. *Opt. Lett.* 35(20):3441–43
145. Cavaletto SM, Buth C, Harman Z, Kanter EP, Southworth SH, et al. 2012. Resonance fluorescence in ultrafast and intense X-ray free-electron-laser pulses. *Phys. Rev. A* 86:033402

146. Weninger C, Rohringer N. 2013. Stimulated resonant X-ray Raman scattering with incoherent radiation. *Phys. Rev. A* 88:053421
147. Kumar Giri S, Saalman U, Rost JM. 2020. Purifying electron spectra from noisy pulses with machine learning using synthetic Hamilton matrices. *Phys. Rev. Lett.* 124:113201
148. Lyu C, Cavaletto SM, Keitel CH, Harman Z. 2020. Narrow-band hard-X-ray lasing with highly charged ions. *Sci. Rep.* 10:9439
149. Simmermacher M, Henriksen NE, Møller KB, Moreno Carrascosa A, Kirrander A. 2019. Electronic coherence in ultrafast X-ray scattering from molecular wave packets. *Phys. Rev. Lett.* 122:073003
150. Bennett K, Biggs JD, Zhang Y, Dorfman KE, Mukamel S. 2014. Time-, frequency-, and wavevector-resolved X-ray diffraction from single molecules. *J. Chem. Phys.* 140:204311
151. Keefer D, Mukamel S. 2021. Selective enhancement of spectroscopic features by quantum optimal control. *Phys. Rev. Lett.* 126:163202